The effect of sheared diamagnetic flow on turbulent structures generated by the Charney–Hasegawa–Mima equation

G. J. J. Botha,[a] M. G. Haines, and R. J. Hastie
Blackett Laboratory, Imperial College, London SW7 2BZ, United Kingdom

(Received 18 May 1999; accepted 21 June 1999)

The generation of electrostatic drift wave turbulence is modeled by the Charney–Hasegawa–Mima equation. The equilibrium density gradient $n_0=n_0(x)$ is chosen so that dn_0/dx is nonzero and spatially variable (i.e., v_{*e} is sheared). It is shown that this sheared diamagnetic flow leads to localized turbulence which is concentrated at $\max(\nabla n_0)$, with a large dv_{*e}/dx inhibiting the spread of the turbulence in the x direction. Coherent structures form which propagate with the local v_{*e} in the y direction. Movement in the x direction is accompanied by a change in their amplitudes. When the numerical code is initialized with a single wave, the plasma behavior is dominated by the initial mode and its harmonics. © *1999 American Institute of Physics.* [S1070-664X(99)00510-8]

I. INTRODUCTION

One of the first characteristics of the H (high) mode that was discovered in tokamaks was the transport barrier at its edge.[1] Since then internal transport barriers have been measured in various machines.[2–5] These barriers (both internal and at the edge) are usually attributed to sheared ($\mathbf{E}\times\mathbf{B}$) flow.[6] However, Shaing *et al.*[7] note that a sheared diamagnetic flow can also suppress turbulence. In this paper, we consider a sheared diamagnetic flow and consider its effect on the turbulence. In order not to complicate our investigation, we choose to include the density profile which generates the diamagnetic flow and suppress other effects.

The numerical model used is the Hasegawa–Mima model of two-dimensional electrostatic drift wave turbulence.[8,9] The model consists of the Charney–Hasegawa–Mima (CHM) equation[10–12] which evolves the perturbed electrostatic potential ϕ_1 while the unperturbed density $n_0=n_0(x)$ is fixed in time with characteristic length $L_n^{-1}=(1/n_0)(dn_0/dx)$. Most numerical simulations (with a few notable exceptions[13,14]) treat L_n^{-1} as a constant and use periodic boundary conditions in both x and y directions on the two-dimensional Cartesian plane. A general review by Arter[15] covers the modeling of drift-wave turbulence in tokamaks using the CHM equation. The present publication considers numerically the influence of various $n_0=n_0(x)$ profiles on the turbulence generated by the CHM equation. In particular, n_0 profiles introducing a sheared diamagnetic flow (v_{*e}) are investigated.

Section II contains a short review of numerical simulations which used the CHM equation. This is followed by Sec. III stating the CHM equation and its two global constants: the generalized energy and the generalized enstrophy. The derivation of the equation and its two global constants, the conditions under which the model is valid as well as the effect of the chosen boundary conditions are discussed in an appendix. In Sec. IV the numerical implementation of this model is described and this is followed by a description of the diagnostics used to present the results (Sec. V). The results obtained in the numerical simulations are divided into three main sections: Section VI describes the coherent structures in the plasma which form in the turbulence; Sec. VII presents the spectra formed by the generalized energy and enstrophy; and Sec. VIII investigates the influence of various density profiles. A summary of all the results concludes this paper.

II. NUMERICAL SIMULATIONS

Most numerical simulations in this field use slab geometry and a two-dimensional regular grid to simulate the plane perpendicular to a constant and uniform magnetic field. The plasma inhomogeneity enters the CHM equation through $L_n^{-1}=(1/n_0)(dn_0/dx)$ with n_0 the equilibrium density. This implies that when L_n^{-1} is zero, a constant or periodic, an infinite plane can be simulated by choosing the boundary conditions periodic in both the x and y directions. In the literature, L_n^{-1} is treated almost exclusively as a constant[16–27] or as equal to zero.[23,28–33] Here, we treat $\rho_s L_n^{-1}\ll 1$, where $\rho_s=c_s/\Omega_{ci}$, c_s being the ion sound speed and Ω_{ci} the ion cyclotron frequency.

Double periodicity allows the numerical codes to be treated spectrally. The modes in the x and y directions range from 16×16 modes[28] to 512×512 modes.[25,26] The existing numerical codes can be divided into spectral codes[17,18,21,22,25,26,28,29] and pseudo-spectral codes.[16,19,20,23,24,27,30–34] In the pseudo-spectral codes, it is usually the linear terms which are calculated in Fourier space, while the nonlinear term is calculated in coordinate space using a finite difference scheme. A few authors have extended this differentiated spatial treatment into the temporal treatment of the CHM equation,[16,20,30] using explicit time steps to advance the linear terms and a split operator Lax–Wendroff scheme[35] for the nonlinear term.

In order to make the numerical simulations become more realistic, the doubly periodic boundary condition needs to be relaxed. Ingersoll and Cuong[13] developed a code which is periodic in the y direction and has $\partial\phi_1/\partial y=0$ along the x boundaries, where ϕ_1 is the field quantity evolved by the CHM equation. Their code is spectral in both the x and y directions with $L_n^{-1}=0$. The nonlinear term is calculated us-

[a]Now at Department of Pure and Applied Physics, Queen's University, Belfast BT7 1NN, UK.

ing Arakawa's scheme[36] in coordinate space and the time scheme uses centered time differences, with a forward integration every fifty time steps.

Su, Horton, and Morrison[14] published results using a numerical code which is periodic only in the y direction. $L_n^{-1}=L_n^{-1}(x)$ implies that the diamagnetic velocity $v_{*e}=-cT_eL_n^{-1}/(eB)$ is sheared. They calculated the nonlinear term in Fourier space and evolved the CHM equation in a space that is spectral in y and finite differenced in x.

Prakash, Chu, and Hasegawa[37] considered a regular grid which is periodic in y and has $\phi_1=0$ on the x boundaries. The nonlinear term was calculated in coordinate space using Arakawa's scheme[36] and the CHM equation was time integrated using the Euler scheme for the first time step and the leapfrog scheme for successive time steps. They used a constant L_n^{-1} (i.e. not a function of time or space) and terminated the numerical run at $T_{\text{fin}}=5\Omega_{ci}^{-1}$, where Ω_{ci} is the ion cyclotron frequency. Such a short run does not allow for the drift-wave turbulence to evolve fully. After reproducing some of their results (Sec. VIII) we extended the duration of our numerical runs to a few characteristic time lengths (Sec. IV).

The duration of the numerical runs varies over a wide range in the published literature. Some simulations are of the order of $10^{-2}\ |L_n|.c_s^{-1}$, while others have a duration of up to[23,20,31] 600 $|L_n|.c_s^{-1}$, 1220 $|L_n|.c_s^{-1}$ and 2000 $|L_n|.c_s^{-1}$. Our numerical runs have durations between 20 $|L_n|.c_s^{-1}$ and 67.4 $|L_n|.c_s^{-1}$ which in each run is enough time for the relevant physics to evolve.

In the literature the following physical effects have been added to the CHM equation: an electron temperature gradient;[14,18,34] a nonlinear term originating from the ($\mathbf{E}\times\mathbf{B}$) velocity;[27] electron dissipation;[18] nonadiabatic electrons;[22] sources and sinks.[22,23,28,31,33] Kawahara *et al.*[24] modified the CHM equation by simplifying the nonlinear term, while many numerical papers included hyperviscosity.[17,25–28,31,32] The accuracy of most numerical codes is measured in terms of conservation of the CHM equation's global constants: the generalized energy and the generalized enstrophy.

All the publications which have been considered in this section, have used Cartesian coordinates with a regular, rectangular numerical grid. This, however, is not the only geometry which is used in the literature. Marcus[38] used plane cylindrical coordinates on an annular grid to study vortex behavior, in order to compare his numerical results with cylindrical laboratory experiments by Sommeria *et al.*[39] Williams[40] used spherical coordinates on a spherical grid in order to simulate Rossby waves in the Jovian atmosphere. He included a force term to introduce vortices with isotropic spectra at a fixed wavenumber.

The research interest of most of the publications can be divided into two main groups: those which are interested in the study of the behavior of coherent vortices in two-dimensional turbulence[13,14,16,17,20,21,23–25,30,31,33,34,38] and those papers which study two-dimensional turbulence itself.[18,19,22,27–29,32,37] This paper presents the effects of a sheared diamagnetic flow on the CHM turbulence and in particular, on the behavior of the coherent structures.

III. THE MODEL

The equation evolved in this model is the Charney–Hasegawa–Mima equation[10–12]

$$\frac{\partial}{\partial t}\left(\frac{e\phi_1}{T_e}-\frac{1}{\Omega_{ci}}\frac{c}{B}\nabla_\perp^2\phi_1\right)-\frac{c}{B}L_n^{-1}\frac{\partial\phi_1}{\partial y}-\frac{1}{\Omega_{ci}}\frac{c^2}{B^2}[\phi_1,\nabla_\perp^2\phi_1]=0 \tag{1}$$

which describes two-dimensional electrostatic turbulence[8,9] on the (x,y) plane perpendicular to a constant and uniform magnetic field $\mathbf{B}=B\hat{z}$. Here, ϕ_1 is the perturbed electrostatic potential, T_e is the constant and uniform electron temperature, e is the electron charge, and c is the speed of light. Ω_{ci} is the ion cyclotron frequency and $L_n^{-1}=(1/n_0)(dn_0/dx)$ is the inverse characteristic length associated with the unperturbed density gradient. The notation [,] represents the Jacobian operator (also known as Poisson brackets).

The Appendix contains a short description of the derivation and validity of the CHM equation and describes how to obtain its two global constants: the generalized energy W and the generalized enstrophy U, defined by

$$W=\int_V\frac{1}{n_0T_e}\left[\frac{1}{2}\frac{n_1^2T_e}{n_0}+\frac{1}{2}m_in_0v_E^2\right]dV, \tag{2}$$

$$U=\int_V\left[\frac{1}{n_0T_e}\left(\frac{1}{2}m_in_0v_E^2\right)+\frac{1}{2}\left(\frac{\nabla\times\mathbf{v}_E}{\Omega_{ci}}\right)^2\right]dV. \tag{3}$$

The influence of the boundary conditions and of $L_n^{-1}=L_n^{-1}(x)$ on W and U is discussed in the Appendix.

IV. THE NUMERICAL IMPLEMENTATION

The two-dimensional domain is divided into a regular grid, the size of one cell (dimensions Δx and Δy) being such that $\Delta x\ll L_n$ and also $\Delta x,\ \Delta y<\rho_s$ where ρ_s is c_s/Ω_{ci}. The dimensions of the numerical domain are given by a_x and a_y in the x and y directions, respectively.

The domain is periodic in the y direction and reflecting boundary conditions[41] at $x=0$ and $x=a_x$ are chosen with $\phi_1=0$. In order to prevent the reflecting boundaries from polluting the numerical solution, ∇n_0 is chosen to be zero next to the x boundaries. This results in $d\phi_1/dx=0$ near the x boundaries which prevents reflection and helps with the conservation of the generalized enstrophy. (The latter is discussed in detail in the Appendix.)

By finite differencing in the x direction and using spectral methods in the y direction, the linear part of the CHM equation may be written as a tridiagonal system describing the evolution of ϕ_1. By using the complex Fourier representation, a bi-tridiagonal system is obtained which evolves the real and imaginary parts of ϕ_1. This system is solved using Von Rosenberg's method.[42] The numerical simulation is dealiazed by setting the top third of the Fourier spectrum to zero. The upper boundary in Fourier space is reflective. The

nonlinear term in the CHM equation is calculated using Arakawa's finite difference scheme for vector nonlinearities.[36]

The CHM equation is time advanced by means of a modified Euler predictor corrector method. If the CHM equation is written symbolically as

$$\frac{\partial Y}{\partial t}+X=Z, \tag{4}$$

where X is the term containing L_n^{-1} and Z is the nonlinear term, then the time advancement scheme is written as

$$Y^{(p)}+X^{(p)}\Delta t=Y^{(t)}+Z^{(t)}\Delta t, \tag{5}$$

$$Y^{(t+1)}+X^{(t+1)}\Delta t=Y^{(t)}+\tfrac{1}{2}[Z^{(t)}+Z^{(p)}]\Delta t, \tag{6}$$

where the superscripts indicate the iteration in time and Δt the time step. The final time T_{fin} and the time step Δt must be chosen so that $\omega_{*e}\Delta t \ll 1$ and $\omega_{*e}T_{\text{fin}} \gg 1$, where $\omega_{*e}=kv_{*e}$, i.e., the time step must be small enough to resolve the physics and the duration of the numerical run must be long enough to cover the time scales of interest. It is useful to define the characteristic time as

$$\frac{1}{kv_{*e}}=\frac{a_y}{mv_{*e}}, \tag{7}$$

where m is the initial mode in Fourier space.

V. DIAGNOSTICS

To obtain a measure of the fluctuations over the computational domain, the definition

$$\left(\frac{e\phi_1}{T_e}\right)_{\text{rms}}=\sqrt{\frac{1}{M}\sum_{j=1}^{M}\left[\frac{e\phi_1(x_i,y_j)}{T_e}\right]^2} \tag{8}$$

is used, where the summation is along the y direction with M the number of grid cells. $(e\phi_1/T_e)_{\text{rms}}$ is a function of x and its x profile may be monitored as it evolves over time. This diagnostic is helpful in observing the level and position of fluctuations along the x axis.

The generalized energy and enstrophy are defined by Eqs. (2) and (3), respectively, and their conservation is the prime indicator of the accuracy of this numerical code. If the definition

$$u=\frac{1}{n_0T_e}\left(\frac{1}{2}m_in_0v_E^2\right)+\frac{1}{2}\left(\frac{\nabla\times\mathbf{v}_E}{\Omega_{ci}}\right)^2 \tag{9}$$

is used, then the generalized enstrophy [Eq. (3)] can be written as

$$U=\int_V u\,dV. \tag{10}$$

The numerical code is spectral in the y direction, which implies that u may be written as

$$u=\sum_{m=-\infty}^{\infty}u_m(x)e^{i2\pi my/a_y}. \tag{11}$$

The x dependence of Eq. (10) then becomes

$$\mathcal{U}_m=\frac{1}{a_x}\int_0^{a_x}u_m(x)dx \tag{12}$$

which allows the monitoring of the different modes of the generalized enstrophy.

By defining

$$w=\frac{1}{n_0T_e}\left(\frac{1}{2}\frac{n_1^2T_e}{n_0}+\frac{1}{2}m_in_0v_E^2\right), \tag{13}$$

$$W=\int_V w\,dV, \tag{14}$$

$$w=\sum_{m=-\infty}^{\infty}w_m(x)e^{i2\pi my/a_y}, \tag{15}$$

$$\mathcal{W}_m=\frac{1}{a_x}\int_0^{a_x}w_m(x)dx, \tag{16}$$

the generalized energy [Eq. (2)] is monitored in a similar way.

VI. COHERENT STRUCTURES

Experimental measurements indicate the possible existence of coherent structures in fusion plasmas.[43,44] By initializing the numerical code with one wave as well with multiple waves in the y direction different turbulent structures are obtained.

The numerical code is initialized with an equilibrium density profile $n_0=n_0(x)$ as shown in Fig. 1. This implies that v_{*e} is sheared along the x direction and is constant in time. The initial perturbation

$$A(x)=\frac{G_0}{\sqrt{2\pi\sigma^2}}\exp\left[\frac{-(x-a_x/2)^2}{2\sigma^2}\right], \tag{17}$$

$$\phi_1(x,y)=A(x)\cos\left(\frac{2\pi my}{a_y}\right) \tag{18}$$

is chosen and with $\sigma=1$ and G_0 a constant, the maximum values of $(kL_n)^{-1}$ and $e\phi_1/T_e$ can be set to occur at the same position on the numerical grid and both are equal to 1.49×10^{-2}. Equation (A5) then implies that the terms in the CHM equation are of comparable magnitude. Two numerical simulations are performed: the first is initialized with a single mode in the y direction ($m=9$), while the second has two initial waves (modes 7 and 11).

The resolution of the numerical grid is the same for both these runs. The y direction has 256 grid cells and a length of $a_y/\rho_s=10/0.43\sim23$, while 85 modes are allowed in Fourier space. During the numerical run initialized with a single mode $a_x\sim28\rho_s$ with 300 grid cells in the x direction and during the run with multiple modes $a_x\sim46.5\rho_s$ with 500 cells.

The duration of the simulations is chosen so that many characteristic times [see Eq. (7)] are fitted into each run. The final time for the simulation initialized with mode 9 is $T_{\text{fin}}=1.4\times10^{-4}$ s$=21|L_n|.c_s^{-1}=8$ characteristic times. Here, the minimum value of $|L_n|$ has been used. The chosen time step is $\Delta t=5\times10^{-9}$ s which gives $\Delta t\omega_{*e}=1.8\times10^{-3}$. The

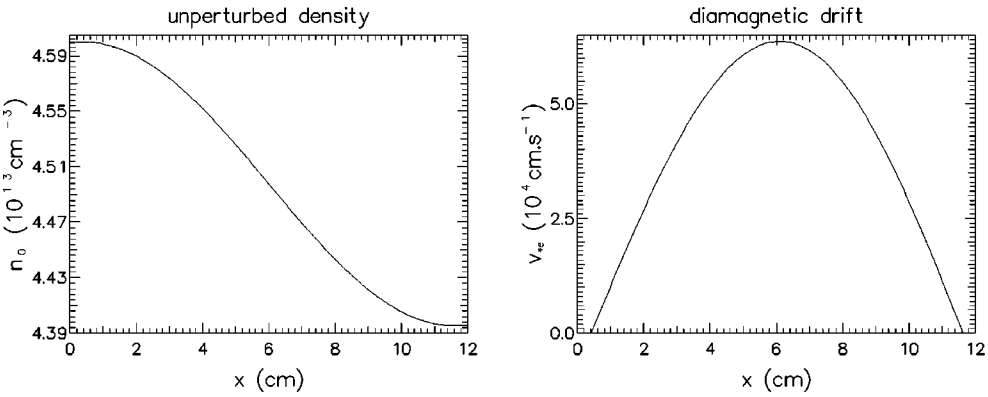

FIG. 1. x profiles of n_0 and v_{*e}.

final time for the simulation with multiple initial modes is $T_{\text{fin}}=4.5\times10^{-4}$ s$=67|L_n|.c_s^{-1}$ which is 20 characteristic times when Eq. (7) uses mode 7 to calculate the characteristic time and T_{fin} is 32 characteristic times when mode 11 is used. The time step $\Delta t=10^{-8}$ s so that $\Delta t\omega_{*e}$ is of the same order as during the simulation initialized with mode 9.

The accuracy of the numerical runs is measured by the conservation of the generalized energy [Eq. (14)] and the generalized enstrophy [Eq. (10)]. During the run initialized with a single mode the change in the generalized energy is less than 0.75%. The generalized enstrophy fluctuates during this run but changes by less than 4%. The change during the run initialized with multiple modes is 1.6% for the generalized energy, while the generalized enstrophy changes by 2.5%.

A. Single mode

The v_{*e} profile creates flows in the y direction which are sheared along the x direction (Fig. 1) with the fastest flow occurring at $x=6$ cm. The effect of this sheared flow is shown in Fig. 2. As early as 2×10^{-5} s after initialization, the numerical simulation evolves into the stable structure, as shown in Fig. 2. During the measurement of Fig. 2 the plasma structures at $x=8.2$ cm moved in the negative y direction at a speed of $1.26v_{*e}$. In contrast to this, the plasma structures at $x=10$ cm show very little movement. Although the shapes of the different substructures change in time, the shape of the main structure in Fig. 2 stays the same.

A Fourier analysis of the temporal fluctuations of $e\phi_1/T_e$ at fixed positions on the numerical grid shows that the frequencies of the faster flows are higher than the frequencies of the slower flows[45] (as expected with the given v_{*e} profile). It also shows that all measured frequencies are of the same order as $\omega_{*e}/2\pi$. The fastest moving plasma at $x=6$ cm has frequencies which are slightly higher than $\omega_{*e}/2\pi$. Closer to the x boundaries where the plasma moves slower in the y direction, the values of the measured frequencies correspond more to their local $\omega_{*e}/2\pi$. A Fourier analysis of the spatial fluctuations gives spectra which show that the initial mode $m=9$ dominates in all the flows along y with the higher harmonics of $m=9$ an order of magnitude smaller.

B. Multiple modes

After 7×10^{-5} s the numerical simulation initialized with modes 7 and 11 has evolved into turbulence which contains coherent structures formed by local maxima and minima on the (x,y) plane. Figure 3 presents contours of $e\phi_1/T_e$ on the (x,y) plane at five different times during the numerical run and is representative of the turbulence from 7×10^{-5} s to T_{fin}. The spatial trajectories of the maxima and minima may be followed as they evolve in time (Figs. 4 and 5, respectively), as well as the time evolution of the amplitudes of these structures (Figs. 6 and 7).

The trajectories of the coherent structures show that the main movement is in the y direction with the y velocities of the same order as their local v_{*e}. This implies that the y trajectories of the coherent structures are longer near $x=a_x/2$ than near the x boundaries (Figs. 4 and 5). Migration in the x direction is more irregular and often accompanied by amplitude changes. This is particularly noticeable for the minima, with a few maxima also showing this behavior (e.g., maximum 3 in Figs. 4 and 6). This behavior is ascribed to the $v_{*e}=v_{*e}(x)$ profile: x movement causes the coherent structures to move through different v_{*e} flows and this causes the amplitude to change. However, this is not the only factor influencing the amplitude of the coherent structures: movement and amplitude changes are influenced by nearby neighbors as well (e.g., minimum 11 in Figs. 5 and 7).

Although the coherent structures on the (x,y) plane were followed for the duration of the numerical simulation, as well as for simulations with different initial modes, no discernible pattern was observed. A minimum and a maximum would join together to form a modon (a pair of extrema of opposite sign) and modons would split up into their two extrema seemingly at random. Sometimes two minima would combine to create one minimum and the same is true for the maxima.

VII. GENERALIZED ENERGY AND ENSTROPHY

The dual cascade model is well established in two-dimensional fluid turbulence[46] and the CHM equation which links this literature with drift wave turbulence has made the

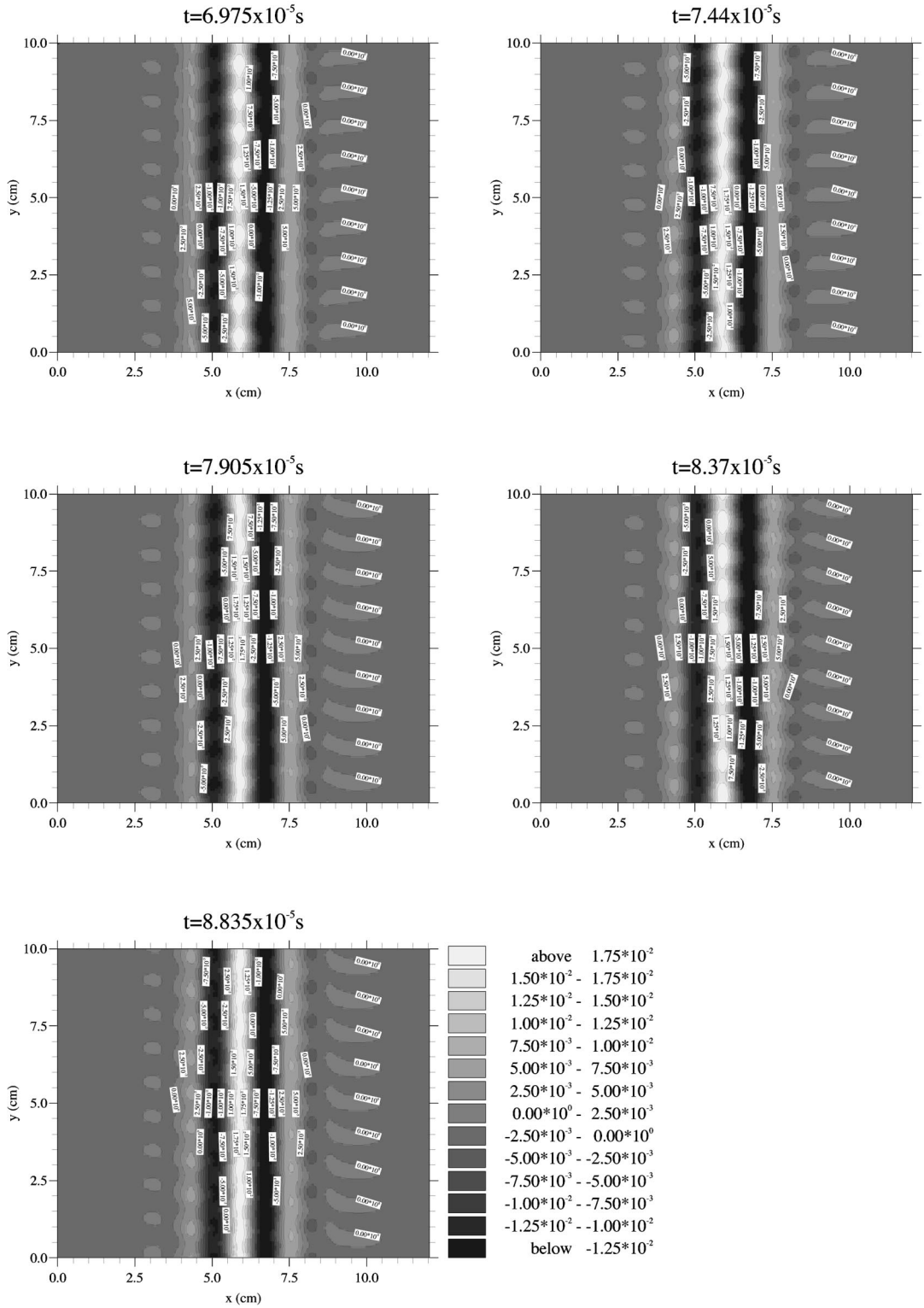

FIG. 2. Contour plots of $e\phi_1/T_e$ as it evolves in time for mode 9.

dual cascade a compelling paradigm in plasma physics.[47] For the parameter space used in this publication, Terry and Newman[48] predict that more than 97% of the generalized energy will cascade to larger scale lengths with the rest cascading to smaller scales. At the same time more than 96% of the generalized enstrophy will cascade to smaller scales with the rest cascading to larger scales. These flows are observed as well as the influence of condensation in the Fourier spectra of the generalized energy and enstrophy. The results presented in this section are obtained with the same initializations as are used in Sec. VI: the first simulation is initialized with mode 9 in Fourier space and the second simulation is initialized with modes 7 and 11. The accuracy of Sec. VI is maintained.

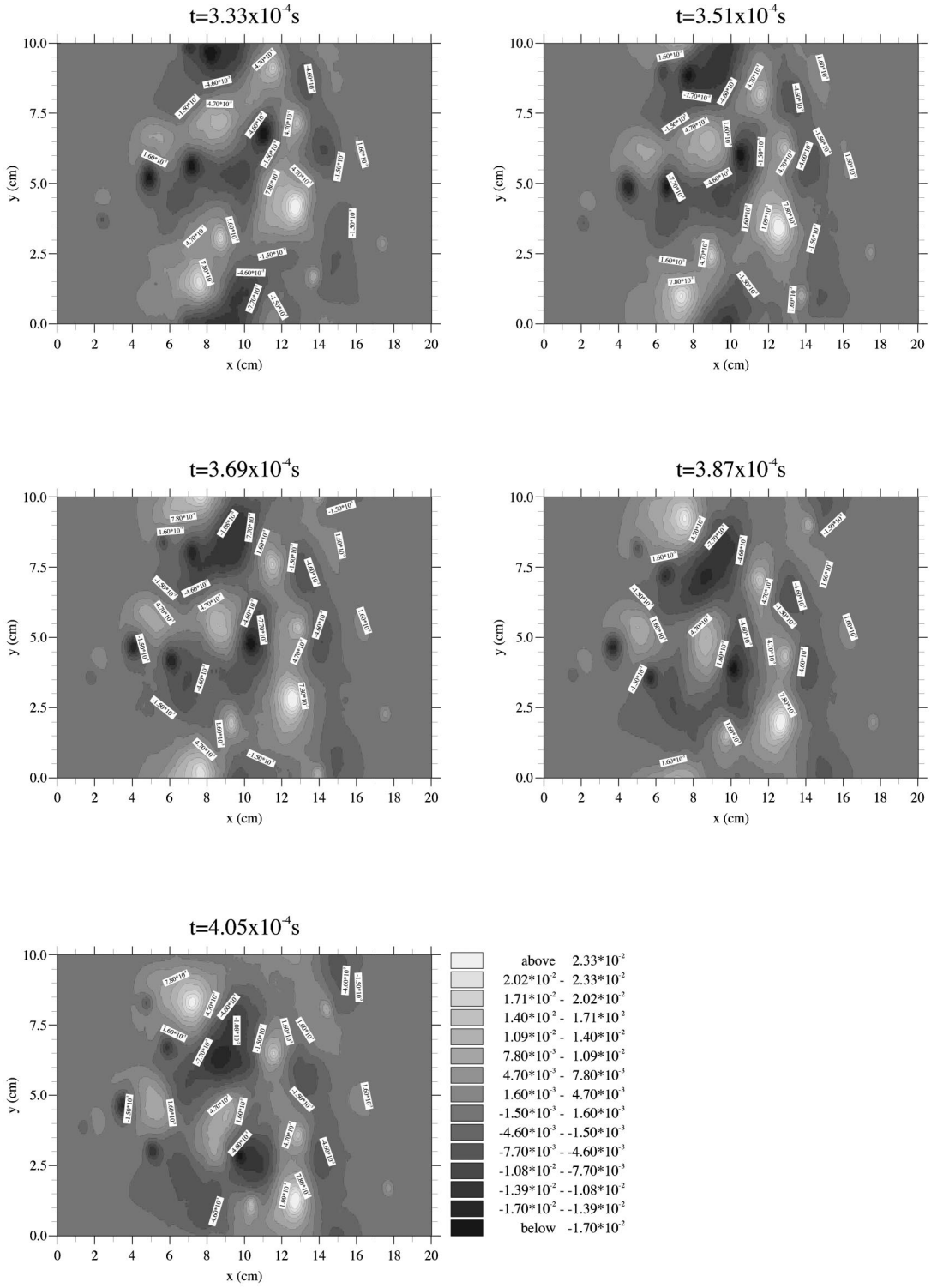

FIG. 3. Contour plots of $e\phi_1/T_e$ as it evolves in time for modes 7 and 11.

A. Single mode

When the numerical simulation is initialized with mode $m=9$ in Fourier space, the initial mode dominates the Fourier spectra of the generalized energy and enstrophy (Figs. 8 and 9, respectively). The initialization first relaxes into a state in which only harmonics of $m=9$ are present. Between 2×10^{-5} and 1.02×10^{-4} s (1.15 and 5.84 characteristic times) a dual cascade involving only these harmonics, saturates and the spectra of $\mathcal{W}_m$ and $\mathcal{U}_m$ show stable behavior. Figure 10 presents the spectra of the generalized energy and enstrophy at 8.091×10^{-5} s and shows that the dual cascade occurs only in harmonics of the initial mode $m=9$. In the generalized energy spectrum, the energy has cascaded mainly to lower mode numbers (larger scale lengths) and has

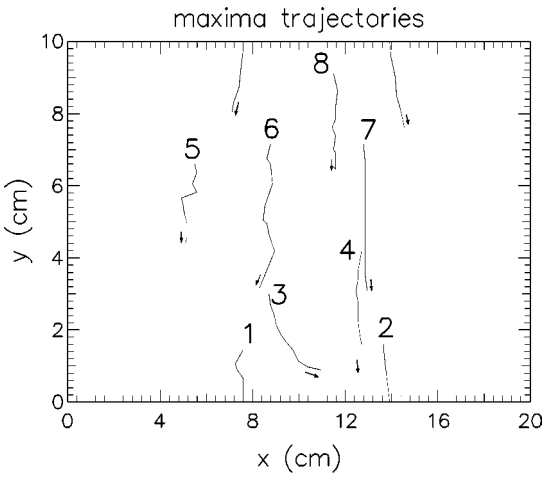

FIG. 4. Spatial trajectories of maxima of $e\phi_1/T_e$ in Fig. 3 as they evolve in time. Each maximum is numbered and the numbers correspond to those in Fig. 6.

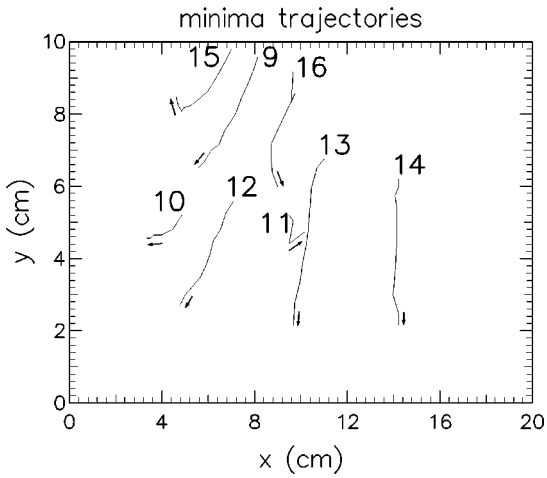

FIG. 5. Spatial trajectories of minima of $e\phi_1/T_e$ in Fig. 3 as they evolve in time. Each minimum is numbered and the numbers correspond to those in Fig. 7.

condensed in mode $m=0$. In the generalized enstrophy spectrum the enstrophy has cascaded to higher mode numbers (smaller scale lengths), while the condensation of the generalized energy at $m=0$ causes the high amplitude of $m=0$ in the generalized enstrophy spectrum. In the same way, the condensation in the higher enstrophy modes is reflected in the generalized energy spectrum (Fig. 8). As can be seen in Figs. 8 and 9, the harmonics of $m=9$ fluctuate in amplitude during the numerical run until 9.765×10^{-5} or $105\times(9.3\times10^{-7})$ s on the time axes of Figs. 8 and 9, after which the stable multiharmonic structure is destroyed by numerical noise. Prior to this transition all the harmonic modes in the generalized enstrophy spectrum gained amplitude as the generalized enstrophy cascaded to higher mode numbers, while the nonharmonic modes grow exponentially from noise until they reach amplitudes comparable with the harmonic modes at 10^{-4} s. All the nonharmonic modes have the same growth rate. A smaller separation between the harmonic modes in the spectrum (e.g., by initializing with $m=3$) or an increased amplitude of the initial perturbation will increase this growth rate. As soon as the nonharmonic and harmonic modes are of comparable amplitude, the stable harmonic structure gives way to turbulence with all m numbers present.

B. Multiple modes

When the simulation is initialized with modes 7 and 11, the initial spectra of the generalized energy ($\mathcal{W}_m$) and the generalized enstrophy ($\mathcal{U}_m$) contain only these two modes. Figure 11 shows the spectra at $t=5.1\times10^{-5}$ s, which is when the plasma enters saturated turbulence and the initial conditions are destroyed. The generalized energy cascades inversely to lower mode numbers, while the generalized enstrophy cascades to higher mode numbers. Unlike the simulation which is initialized with mode 9 only, the modes which are generated do not belong only to the harmonics of modes 7 and 11. Figure 11 also shows that the condensation at the lower modes of the $\mathcal{W}_m$ spectrum manifests in the high amplitudes of the lower modes in the $\mathcal{U}_m$ spectrum, while Terry and Newman[48] predict very little inverse cascading for $\mathcal{U}_m$. The reason for this is that they assume no condensation in the spectra.

After $t=5.1\times10^{-5}$ s the shapes of the spectra stay largely the same until the end of the numerical run, while the individual modes change as they evolve in time. In the $\mathcal{W}_m$ spectrum the lower modes grow. In contrast to this, the lower modes in the $\mathcal{U}_m$ spectrum diminish and all the higher modes

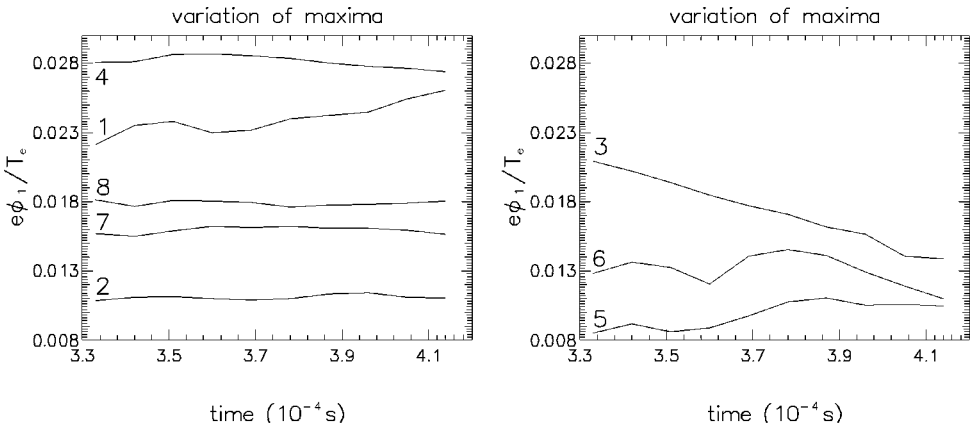

FIG. 6. Time evolution of the amplitudes of the maxima of $e\phi_1/T_e$. Each maximum is numbered and the numbers correspond to those in Fig. 4.

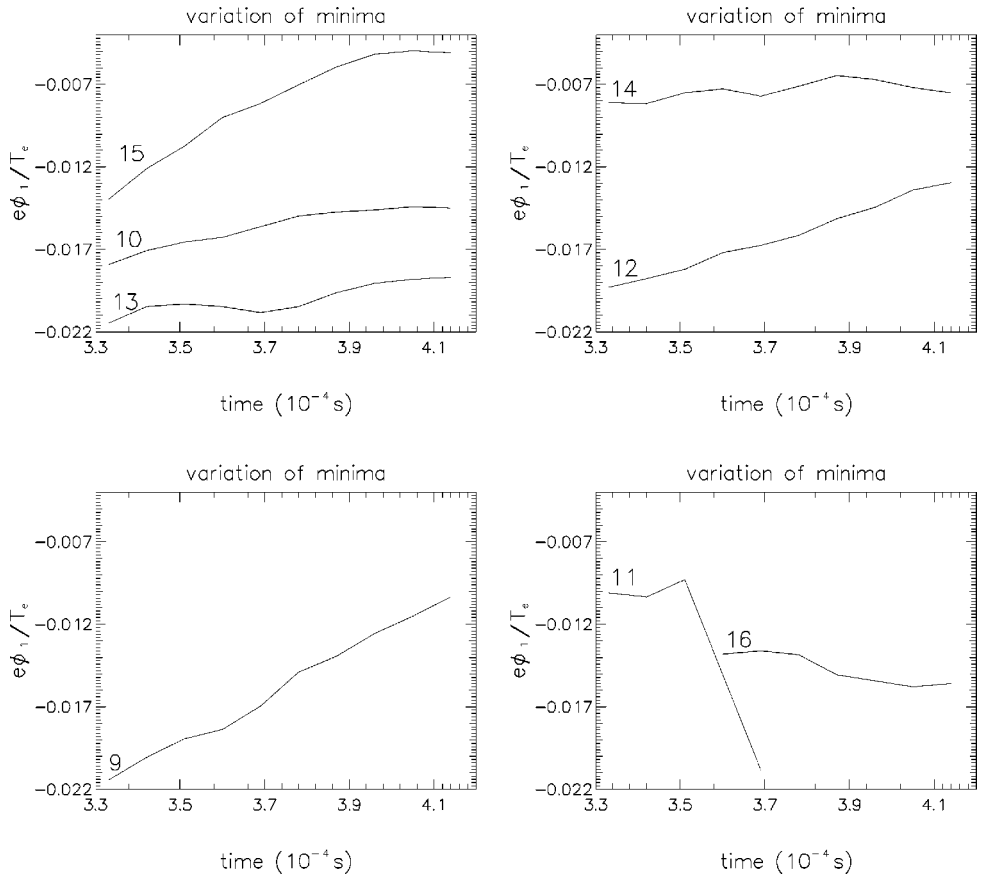

FIG. 7. Time evolution of the amplitudes of the minima of $e\phi_1/T_e$. Each minimum is numbered and the numbers correspond to those in Fig. 5.

increase in amplitude as the generalized enstrophy continuously flows to higher modes. The upper boundary in Fourier space is reflective to facilitate generalized enstrophy conservation. This reflective boundary causes the growing amplitudes of $\mathcal{U}_m$ for high m numbers, as the simulation progresses in time.

The spectra at the end of the simulation (T_{fin}) are presented in Fig. 12. At T_{fin} modes 1, 2, and 3 dominate the $\mathcal{W}_m$ spectrum with mode $m=2$ having the largest amplitude. Drift wave ordering [Eq. (A2)] gives $m=a_y/(2\pi\rho_s)\sim 4$ using the initialization values. None of this is reflected in the $\mathcal{W}_m$ spectrum because the condensation in the lower modes

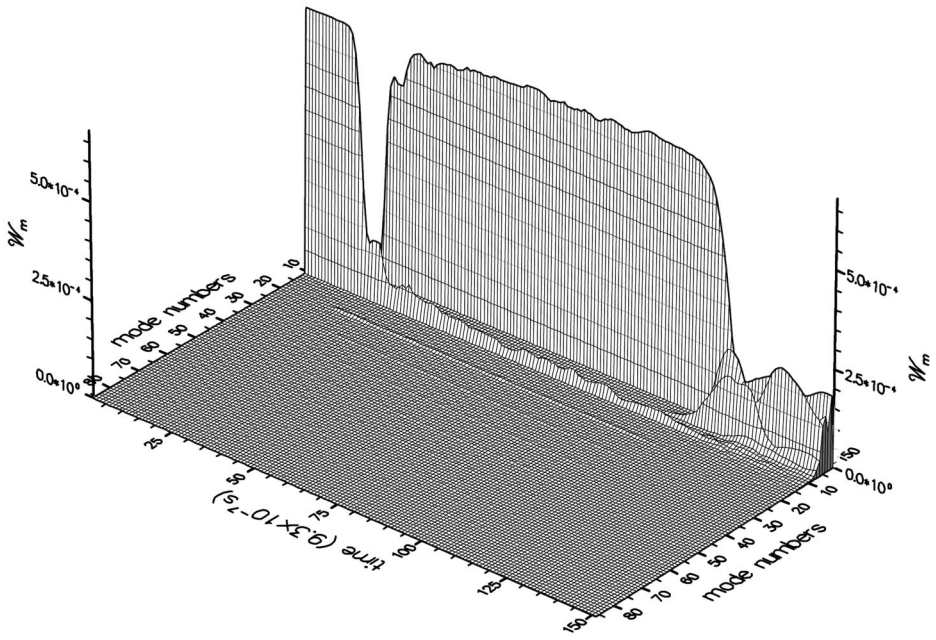

FIG. 8. Time evolution of $\mathcal{W}_m$ during numerical run initialized with mode 9.

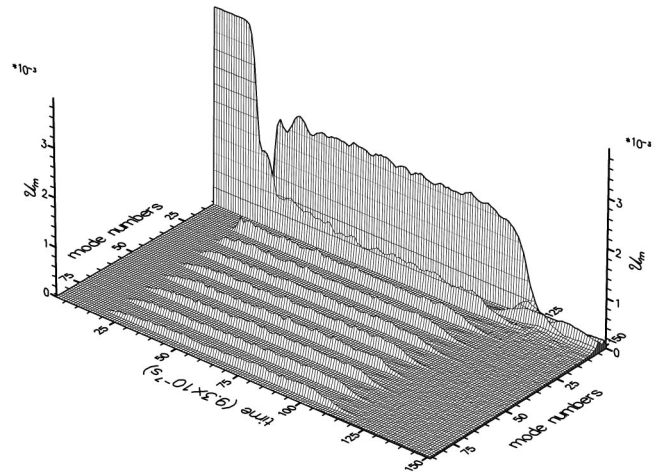

FIG. 9. Time evolution of $\mathcal{U}_m$ during numerical run initialized with mode 9.

dominates all other spectral structure. The final $\mathcal{U}_m$ spectrum of the simulation is influenced by the final $\mathcal{W}_m$ spectrum in that the same modes which are dominant in $\mathcal{W}_m$ have the largest amplitudes in the $\mathcal{U}_m$ spectrum.

VIII. AMPLITUDE OF THE SHEARED DIAMAGNETIC FLOW

In order to study the effect of the size of dv_{*e}/dx on the plasma turbulence, the numerical code is initialized with different profiles of $n_0=n_0(x)$.

A. The n_0 profile in Fig. 1

By choosing a spatially uniform and nonvariable L_n^{-1}, the numerical results obtained with this code may be compared to the results published by Prakash, Chu, and Hasegawa.[37] By considering the behavior directly after initialization, their nonlinear results which describe symmetric propagation along the x direction of W_x are reproduced by this numerical code—but not their asymmetric propagation of the pulse. Our initial pulse propagates at equal rates to both x boundaries and when it reaches these boundaries, it is reflected back towards the center of the x axis and in doing so contaminates the numerical solution in the domain. This reflection is eliminated by introducing an $L_n^{-1}=L_n^{-1}(x)$ profile (Fig. 1) so that $v_{*e}=0$ at the x boundaries and a maximum at $a_x/2$. This enables the duration of the numerical runs to be lengthened while the turbulence is kept away from the x boundaries. Again no significant asymmetry in the propagation along the x direction is found.

Figure 13 contains the x distributions of $(e\phi_1/T_e)_{\rm rms}$ and it shows that the initial perturbation is a Gaussian in the middle of the x axis and away from the x boundaries. As time evolves, the perturbation moves towards the x boundaries and at $T_{\rm fin}$ the perturbation is a distance $0.9\rho_s$ away from both x boundaries.

B. The n_0 profiles in Figs. 14 and 15

Different $n_0=n_0(x)$ profiles are used to initialize two separate numerical simulations. One is in the form of a step function (Fig. 14) and the other of a top hat function (Fig. 15). In both cases, the sharp edges are smoothed out and dn_0/dx are finite. These n_0 profiles will be referred to as the ''step'' and the ''top hat'' profiles, respectively. Figures 14 and 15 also present profiles of $|kL_n|^{-1}$, where k has been calculated using Eq. (A2). They show that $dn_0/dx=0$ for $x\in(0,0.9\rho_s)$, $x\in(32.6\rho_s,51\rho_s)$ and $x\in(82.8\rho_s,83.7\rho_s)$, i.e., exactly in the middle of the x axis and at the x boundaries. The $|kL_n|^{-1}$ profiles also indicate that two main streams form in the plasma, flowing with the local v_{*e} along the y direction. Table I presents a summary of these streams.

The resolution of the numerical grid is the same as during the previous simulations. The length of the x axis is now chosen to be $a_x=83.7\rho_s$ and the number of grid cells in this direction to be 900. The time step $\Delta t=7.5\times10^{-9}$ s and the final time is $T_{\rm fin}=4.5\times10^{-4}$ s$=67|L_n|.c_s^{-1}$ calculated with $\min|L_n|$. This gives 20 characteristic times for mode 7 and 32 characteristic times for mode 11 in each plasma stream.

The initial ϕ_1 perturbation is similar to Eqs. (17) and (18) when multiple modes in Fourier space are used, except that two normal distributions are fitted along the x direction: each has $\sigma=1$ and their maxima are at $x=10$ cm$=23.3\rho_s$ and $x=26$ cm$=60.5\rho_s$. These maxima are therefore an equal distance away from $a_x/2$ as well as from the x boundaries. The sizes of the maxima are such that the linear and nonlinear terms in the CHM equation are of comparable magnitude [according to Eq. (A5)].

With this initialization, a high level of accuracy is maintained during the numerical simulations. The generalized en-

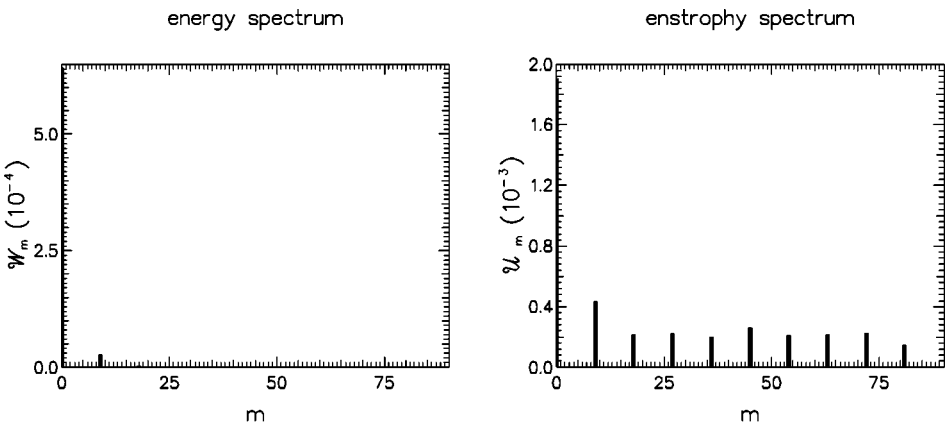

FIG. 10. Generalized energy and enstrophy spectra at $t=8.091\times10^{-5}$ s, which is $87\times(9.3\times10^{-7})$ s on the time axes of Figs. 8 and 9.

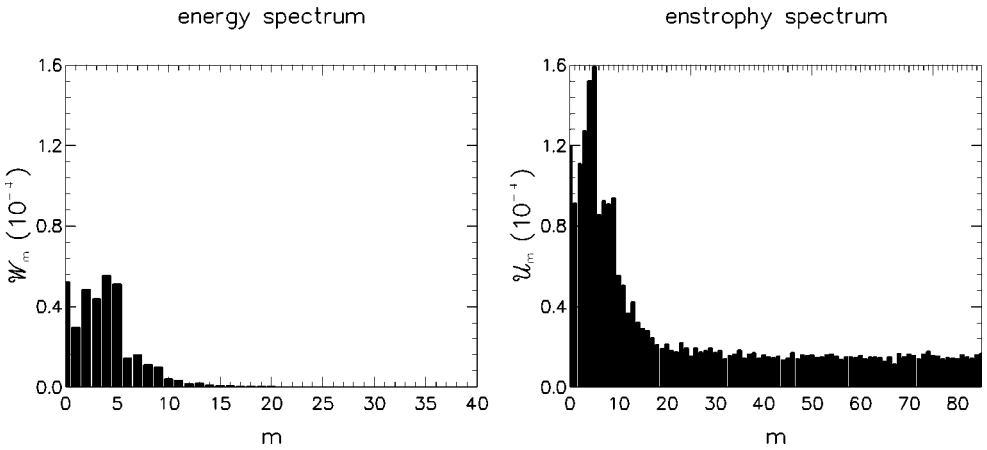

FIG. 11. Generalized energy and enstrophy spectra at $t=5.1\times10^{-5}$ s for the numerical runs initialized with modes 7 and 11.

ergy shows a loss of 1% during both simulations while the change in the generalized enstrophy is 1.4% and 2%, respectively, when the step and the top hat profiles are used.

Figures 16 and 17 present the x distribution of $(e\phi_1/T_e)_{\rm rms}$ as measured at different times during these numerical simulations. The initial symmetry in the x distribution of $(e\phi_1/T_e)_{\rm rms}$ is largely maintained during the numerical simulation which uses the top hat profile (Fig. 16). In contrast to this, during the numerical simulation using the step profile (Fig. 17), a stronger perturbation moves from 10 cm into the region where $dn_0/dx=0$ than from 26 cm. This is shown by the fact that the fluctuations in the region $x\in(14\text{ cm}, 22\text{ cm})$ are larger near 14 cm than near 22 cm.

From this observation it is deduced that the size of the gradient of v_{*e} influence the spread of the perturbation in the x direction. During the numerical run which uses the step profile, the v_{*e} flow at $x=28.9$ cm is larger than the flow at $x=7.3$ cm (Table I). This implies that dv_{*e}/dx is also larger and this steeper gradient inhibits the spread of the turbulence in the x direction in the stream at $x=28.9$ cm more effectively than in the case of the stream at $x=7.3$ cm. This can be seen in the x dependence of $(e\phi_1/T_e)_{\rm rms}$ measured at $t=3\times10^{-4}$ s in Fig. 17: in the faster flowing stream, the turbulence is still 1.2 cm away from the $x=36$ cm boundary, while the turbulence in the slower flowing stream is almost at the $x=0$ boundary. During the numerical run which uses the top hat profile, the two v_{*e} flows have the same size and the fluctuations in both flows are the same distance away from the x boundaries at time $t=3\times10^{-4}$ s (Fig. 16).

This result is not inconsistent with Wakatani *et al.*[47] who had a resistive model which contained diamagnetic as well as sheared $(\mathbf{E}\times\mathbf{B})$ flows. They showed that it is mainly the diamagnetic flow that is responsible for the level of saturated fluctuations, while the sign of the $(\mathbf{E}\times\mathbf{B})$ flow influences the level of fluctuations during the growth phase. We find that a sheared diamagnetic flow $|dv_{*e}/dx|$ inhibits the spreading of the saturated fluctuations in the x direction.

IX. SUMMARY

In this publication turbulence is generated using the CHM equation with $dL_n^{-1}/dx\neq0$. As is expected from two-dimensional turbulence, the spectra of the generalized energy and enstrophy show that the generalized energy flows to larger and the generalized enstrophy to smaller spatial structures. In all cases, the generalized energy condensates in the

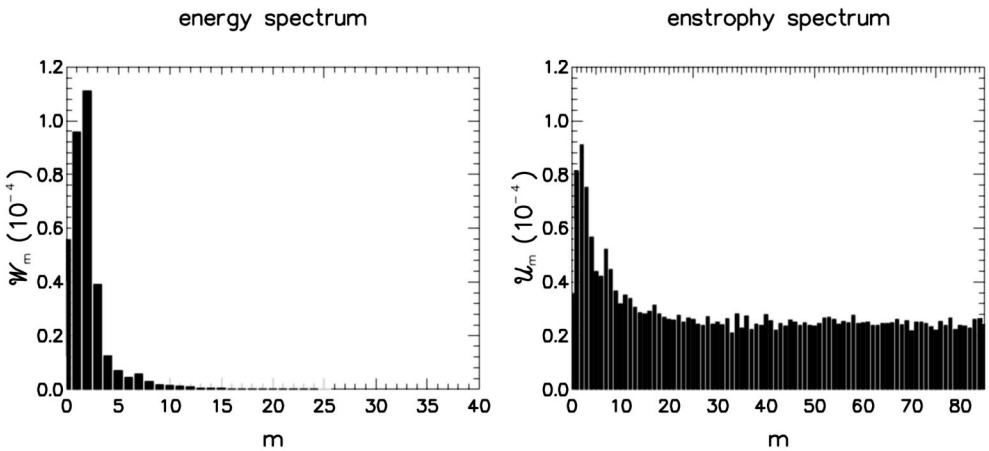

FIG. 12. Generalized energy and enstrophy spectra at $T_{\rm fin}$ for the numerical runs initialized with modes 7 and 11.

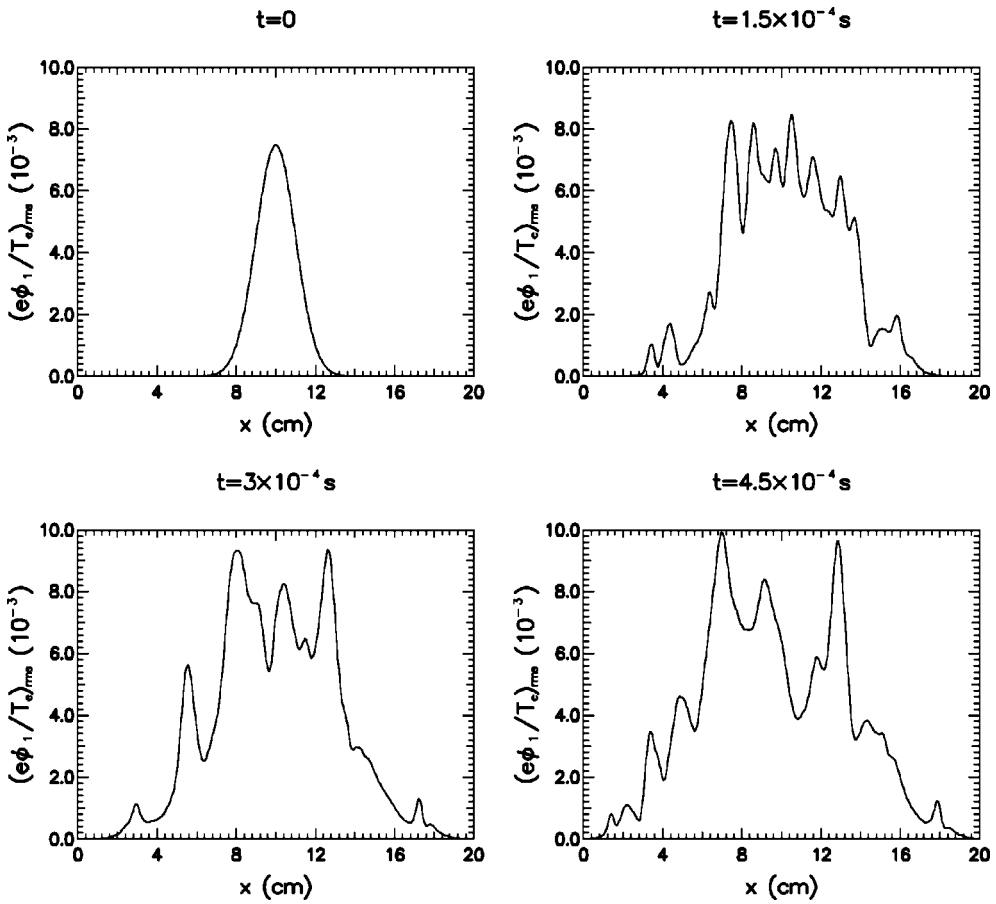

FIG. 13. x profiles of $(e\phi_1/T_e)_{\rm rms}$ at four different times during simulation when the n_0 profile of Fig. 1 is used.

lower part of its spectrum and this causes high amplitudes in the lower part of the generalized enstrophy spectrum in spite of the enstrophy flowing to higher modes.

When the numerical code is initialized with one harmonic in the y direction (i.e., a single mode in its generalized energy and enstrophy spectra), a stable structure temporarily forms in the (x,y) plane. This structure consists of different streams which flow in the direction of the diamagnetic velocity, each flow corresponding to the local v_{*e} and with a spatial spectrum dominated by the initial mode.

For the single mode initialization, the spectrum of the generalized energy shows that the energy flow to lower modes is restricted at first to the initial mode and its harmonics. Similarly, in the generalized enstrophy spectrum, the enstrophy flows exclusively to modes that are higher harmonics of the initial mode. After a significant number of characteristic times this nonlinear state, which is dominated by its initial conditions, is destroyed by growing nonharmonic modes to evolve into a fully turbulent state with all m numbers present.

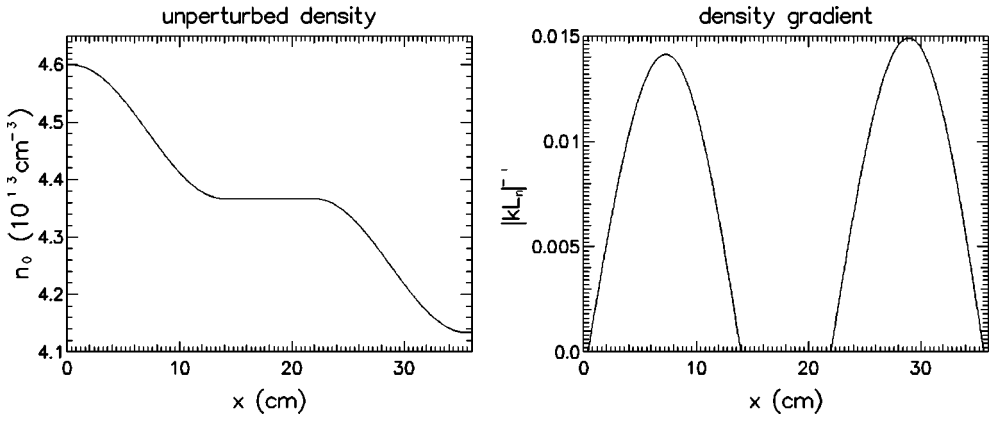

FIG. 14. Unperturbed density profile which resembles a step function.

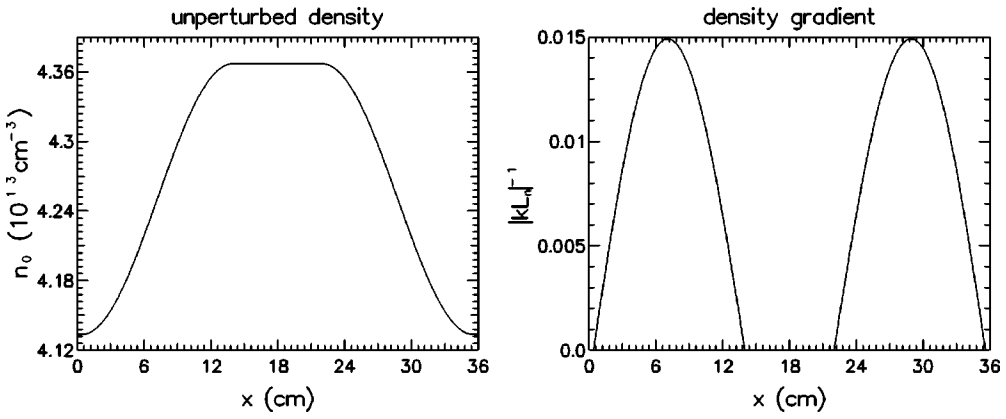

FIG. 15. Unperturbed density profile which resembles a top hat function.

When the numerical code is initialized with multiple modes in the y direction (i.e., multiple modes in its generalized energy and enstrophy spectra), the two-dimensional turbulence saturates shortly after initialization and local maxima and minima form in the turbulence. These extrema propagate mainly in the direction of the diamagnetic flow with a speed of the same order as the local v_{*e}. Some migration in the x direction is observed, which is accompanied by changes in the amplitudes of the extrema. This is explained by the fact that the maxima and minima sample the value of the local $v_{*e}=v_{*e}(x)$.

For the multiple mode initialization, the generalized energy flows to lower modes utilizing all the modes in its spectrum—irrespective of the initial condition. The same is true for the generalized enstrophy spectrum where the enstrophy flows to higher modes.

The effect of the size of dv_{*e}/dx on the turbulence generated by the CHM equation has been investigated. Although ∇n_0 (and hence v_{*e}) is the source of the turbulence, it is shown that the larger dv_{*e}/dx is, the more the turbulence is prevented from spreading in the x direction. This is explained by postulating that the shear in v_{*e} tears the turbulence and thus inhibits its spread in the x direction. The same mechanism may be at work in the measured transport barriers in experiments: the sheared ($\mathbf{E}\times\mathbf{B}$) flow breaks the turbulence up and reduces the transport across these barriers. Although no transport has been calculated in this publication, it is hoped that by showing the influence of $v_{*e}=v_{*e}(x)$ on electrostatic turbulence, we can contribute to the understanding of the mechanism active in transport barriers.

APPENDIX A: THE FIELD EQUATION AND ITS PROPERTIES

1. The field equation

The Hasegawa–Mima model for plasma turbulence[8,9] is a two-dimensional model describing turbulence on the (x,y) plane perpendicular to a constant and uniform magnetic field $\mathbf{B}=B\hat{z}$. The electric field is $\mathbf{E}=-\nabla\phi_1$, where ϕ_1 is the perturbed electrostatic potential. The electrons have a constant and uniform temperature T_e and are assumed to be in thermal equilibrium along the magnetic field lines. Consequently, the electron physics is described by the adiabatic response $n_1/n_0=e\phi_1/T_e$ along each magnetic field line, where e is the electron charge and n_1 and $n_0=n_0(x)$ are the perturbed and equilibrium densities. The ions are cold and are described by the fluid equation of continuity which contains only the ($\mathbf{E}\times\mathbf{B}$) and the polarization velocities. Substituting the adiabatic response into the ion equation of continuity by invoking quasineutrality and using the orderings

$$\frac{e\phi_1}{T_e}\ll 1; \quad \rho_s L_n^{-1}\ll 1 \tag{A1}$$

as well as the drift wave ordering

$$\rho_s k\sim O(1), \tag{A2}$$

the Charney–Hasegawa–Mima (CHM) equation[10–12]

$$\frac{\partial}{\partial t}\left(\frac{e\phi_1}{T_e}-\frac{1}{\Omega_{ci}}\frac{c}{B}\nabla_\perp^2\phi_1\right)-\frac{c}{B}L_n^{-1}\frac{\partial\phi_1}{\partial y}$$

$$-\frac{1}{\Omega_{ci}}\frac{c^2}{B^2}[\phi_1,\nabla_\perp^2\phi_1]=0 \tag{A3}$$

is obtained, where

$$[\phi_1,\nabla_\perp^2\phi_1]=\frac{\partial\phi_1}{\partial x}\frac{\partial\nabla_\perp^2\phi_1}{\partial y}-\frac{\partial\nabla_\perp^2\phi_1}{\partial x}\frac{\partial\phi_1}{\partial y}. \tag{A4}$$

The notation $\rho_s=c_s/\Omega_{ci}$ is used where c_s is the sound speed as well as $L_n^{-1}=(1/n_0)(dn_0/dx)$ which is the inverse characteristic length associated with the unperturbed density gradient.

When the linear term containing L_n^{-1} is of the same size as the nonlinear term in Eq. (A3),

TABLE I. Different streams flowing with velocity v_{*e}.

Profile	Local max$\lvert v_{*e}\rvert$	x position	Flow direction
Step	6.003×10^4 cm s^{-1}	7.3 cm	positive y axis
	6.333×10^4 cm s^{-1}	28.9 cm	positive y axis
Top hat	6.333×10^4 cm s^{-1}	7.1 cm	negative y axis
	6.333×10^4 cm s^{-1}	28.9 cm	positive y axis

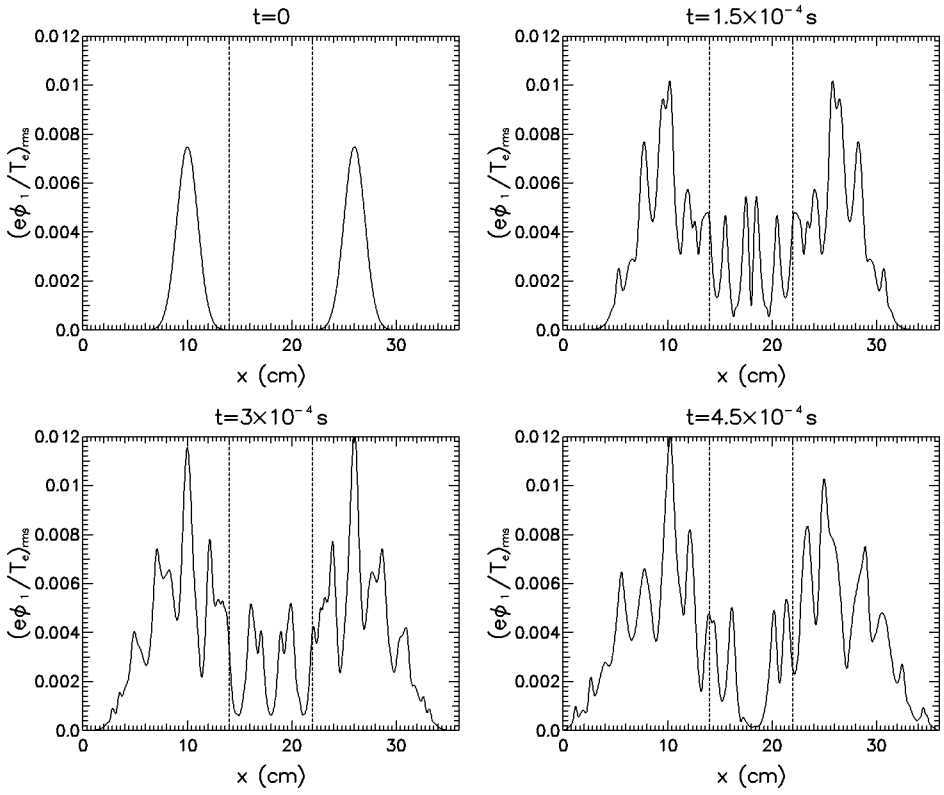

FIG. 16. x profiles of $(e\phi_1/T_e)_{\rm rms}$ at four different times during simulation using top hat profile.

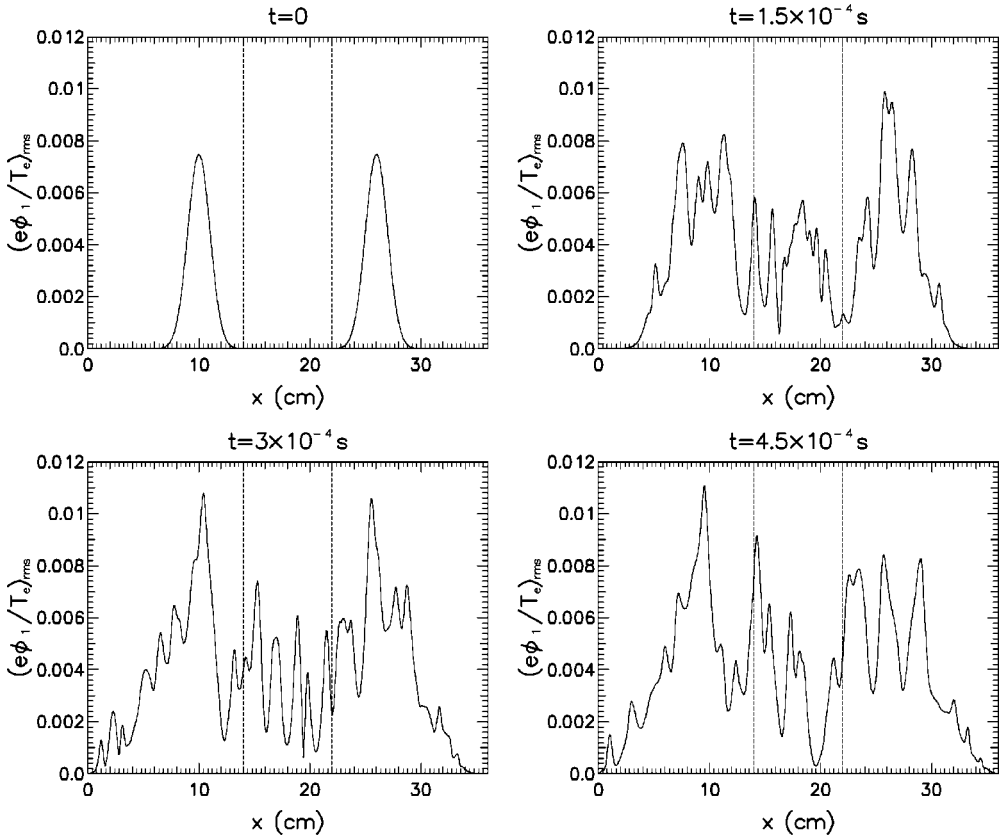

FIG. 17. x profiles of $(e\phi_1/T_e)_{\rm rms}$ at four different times during simulation using step profile.

$$(kL_n)^{-1} \sim \frac{e\phi_1}{T_e} \tag{A5}$$

is obeyed. From Eqs. (A1) and (A2) it follows that the CHM equation is valid only when $(kL_n)^{-1} \ll 1$. Equation (A5) is therefore consistent with Eqs. (A1) and (A2). It should be noted that these orderings have nothing to say about the variation of $L_n^{-1} = L_n^{-1}(x)$. The scale at which L_n^{-1} changes in the x direction (i.e., dL_n^{-1}/dx) does not enter the derivation of the CHM equation and consequently $d^2 n_0/dx^2$ is not relevant when deciding the validity of the equation.

2. Constants of motion

To obtain the local conservation property of the CHM equation, Eq. (A3) is written as

$$\left(\frac{\partial}{\partial t} + \mathbf{v}_E \cdot \nabla\right) \Phi = 0, \tag{A6}$$

$$\Phi = \ln n_0 + \frac{e\phi_1}{T_e} - \frac{1}{\Omega_{ci}} \frac{c}{B} \nabla^2 \phi_1 . \tag{A7}$$

Thus, Φ (known as the potential vorticity[23]) is conserved along the trajectory of a fluid element. This local conservation property gives rise to an infinite family of invariants which may be obtained by considering any function of Φ along the line of flow of a fluid element.

The CHM equation also possesses global integral invariants which are not obtained from the conservation of Φ.[49] Of all the invariants, only two of the non-Φ invariants are conserved if the Fourier spectrum is truncated to a finite number of modes: the generalized energy and the generalized enstrophy. These two global constants are the topic of the next section.

3. Global constants

In contrast to the published literature where they usually are derived with $L_n^{-1} = 0$ or constant, the generalized energy and enstrophy will be derived with $L_n^{-1} = L_n^{-1}(x)$.

The generalized energy is obtained by multiplying Eq. (A3) by $e\phi_1/T_e$ and then integrating it over the volume. This results in

$$\frac{\partial W}{\partial t} + \int_V \frac{v_{*e}}{2} \frac{\partial}{\partial y} \left(\frac{e\phi_1}{T_e}\right)^2 dV + \int_S \mathbf{J}_1 \cdot \mathbf{dS} = 0, \tag{A8}$$

where v_{*e} is the electron density gradient drift (also known as the diamagnetic velocity) and

$$W = \int_V \frac{1}{n_0 T_e} \left[\frac{1}{2} \frac{n_1^2 T_e}{n_0} + \frac{1}{2} m_i n_0 v_E^2\right] dV, \tag{A9}$$

$$\mathbf{J}_1 = \frac{-1}{\Omega_{ci}} \frac{ec}{BT_e} \phi_1 \frac{\partial}{\partial t} \nabla \phi_1 + \frac{1}{\Omega_{ci}} \frac{ec^2}{T_e B^2} \phi_1 \nabla_\perp^2 \phi_1 \times (\nabla \phi_1 \times \hat{z}). \tag{A10}$$

Equation (A9) is identified as a generalized energy (consisting of pressure and kinetic energy terms) and the third term in Eq. (A8) as an energy flux. The volume integral in Eq. (A8) is a source or a sink of the generalized energy.

The generalized enstrophy is obtained by multiplying Eq. (A3) by $c/(\Omega_{ci} B) \nabla^2 \phi_1 = \rho_s^2 \nabla^2 (e\phi_1/T_e)$ and then integrating it over the volume. This process results in

$$\frac{\partial U}{\partial t} + \int_V \left[\rho_s^2 \frac{\partial}{\partial x}\left(\frac{e\phi_1}{T_e}\right) \frac{\partial}{\partial y}\left(\frac{e\phi_1}{T_e}\right) \frac{dv_{*e}}{dx} + \frac{v_{*e}}{2} \frac{\partial}{\partial y}\left(\rho_s \nabla \frac{e\phi_1}{T_e}\right)^2\right] dV + \int_S \mathbf{J}_2 \cdot \mathbf{dS} = 0, \tag{A11}$$

where

$$U = \int_V \left[\frac{1}{n_0 T_e}\left(\frac{1}{2} m_i n_0 v_E^2\right) + \frac{1}{2}\left(\frac{\nabla \times \mathbf{v}_E}{\Omega_{ci}}\right)^2\right] dV, \tag{A12}$$

$$\mathbf{J}_2 = \frac{c^2}{B^2} \frac{1}{\Omega_{ci}} L_n^{-1} \nabla \phi_1 \frac{\partial \phi_1}{\partial y} - \frac{1}{\Omega_{ci}} \frac{ec}{BT_e} \nabla \phi_1 \frac{\partial \phi_1}{\partial t} - \frac{1}{\Omega_{ci}^2} \frac{c^3}{B^3} \frac{1}{2} (\nabla^2 \phi_1)^2 (\nabla \phi_1 \times \hat{z}). \tag{A13}$$

Equation (A12) is identified as the generalized enstrophy (consisting of a kinetic and a vorticity term) and the last term in Eq. (A11) as the generalized enstrophy flux. The volume integral in Eq. (A11) defines a source or a sink.

4. Boundary conditions and the global constants

The geometry used in the numerical simulations is that of a two-dimensional slab in Cartesian coordinates. The slab is periodic in the y direction and at the two boundaries at $x = 0$ and $x = a_x$ the perturbed electrostatic potential $\phi_1 = 0$. Here, a_x is the length of the slab in the x direction.

Equation (A8) describes the evolution of the generalized energy W. The periodicity in y makes the volume integral in Eq. (A8) identically zero, while the energy flux vanishes under the influence of the x and y boundary conditions. Equation (A8) therefore reduces to

$$\frac{\partial W}{\partial t} = 0 \tag{A14}$$

which implies that the generalized energy is conserved by these boundary conditions.

Equation (A11) describes the evolution of the generalized enstrophy U. The volume integral in Eq. (A11) vanishes due to the periodicity in y. $\mathbf{J}_2$ consists of three terms, the first two of which are periodic in y and vanish at $x = 0$ and $x = a_x$. As a result the first two terms in the surface integral of Eq. (A11) vanish. When the third term of $\mathbf{J}_2$ is written in component form, it becomes clear that the x component vanishes due to the periodicity in y while the y component is nonzero. Hence Eq. (A11) reduces to

$$\frac{\partial U}{\partial t} + \frac{1}{\Omega_{ci}^2} \frac{c^3}{B^3} \frac{1}{2} \int_y \left(\frac{\partial^2 \phi_1}{\partial x^2}\right)^2 \frac{\partial \phi_1}{\partial x} \frac{dy}{a_y} = 0 \tag{A15}$$

which means that the generalized enstrophy will be conserved only when either

$$\frac{\partial \phi_1}{\partial x} = 0 \quad \text{or} \quad \frac{\partial^2 \phi_1}{\partial x^2} = 0 \tag{A16}$$

at the x boundaries. Note that $L_n^{-1} = L_n^{-1}(x)$ does not influence the conservation properties of the generalized enstrophy. In this paper the x boundary condition is $\phi_1 = 0$. At the same time ϕ_1 is monitored so that $d\phi_1/dx = 0$ near the x boundaries. It follows that the generalized enstrophy is conserved during the numerical simulations.

[1] F. Wagner, G. Fussmann, T. Grave *et al.*, Phys. Rev. Lett. **53**, 1453 (1984).
[2] E. J. Strait, L. L. Lao, M. E. Mauel *et al.*, Phys. Rev. Lett. **75**, 4421 (1995).
[3] H. Kimura and the JT-60 Team, Phys. Plasmas **3**, 1943 (1996).
[4] L. L. Lao, K. H. Burrel, T. S. Casper *et al.*, Phys. Plasmas **3**, 1951 (1996).
[5] E. Mazzucato, S. H. Batha, M. Beer *et al.*, Phys. Rev. Lett. **77**, 3145 (1996).
[6] K. H. Burrell, Phys. Plasmas **4**, 1499 (1997).
[7] K. C. Shaing, E. C. Crume, and W. A. Houlberg, Phys. Fluids B **2**, 1492 (1990).
[8] P. C. Liewer, Nucl. Fusion **25**, 543 (1985).
[9] W. Horton, Phys. Rep. **192**, 1 (1990).
[10] J. G. Charney, ''On the scale of atmospheric motions,'' in *Geofysiske publikasjoner* (Det norske videnskaps akademi i Oslo, 1948), Vol. 17, No. 2.
[11] A. Hasegawa and K. Mima, Phys. Rev. Lett. **39**, 205 (1977); Phys. Fluids **21**, 87 (1978).
[12] A. Hasegawa, C. G. Maclennan, and Y. Kodama, Phys. Fluids **22**, 2122 (1979).
[13] A. P. Ingersoll and P. G. Cuong, J. Atmos. Sci. **38**, 2067 (1981).
[14] X. N. Su, W. Horton, and P. J. Morrison, Phys. Fluids B **3**, 921 (1991).
[15] W. Arter, Rep. Prog. Phys. **58**, 1 (1995).
[16] M. Makino, T. Kamimura, and T. Taniuti, J. Phys. Soc. Jpn. **50**, 980 (1981).
[17] T. Taniuti and A. Hasegawa, Phys. Scr. **T2/2**, 529 (1982).
[18] P. W. Terry and W. Horton, Phys. Fluids **26**, 106 (1983).
[19] W. Horton, Phys. Fluids **29**, 1491 (1986).
[20] M. Kono and E. Miyashita, Phys. Fluids **31**, 326 (1988).
[21] W. Horton, Phys. Fluids B **1**, 524 (1989).
[22] A. B. Mikhailovskii, A. M. Pukhov, and O. G. Onishchenko, Phys. Lett. A **141**, 154 (1989).
[23] J. A. Crotinger and T. H. Dupree, Phys. Fluids B **4**, 2854 (1992).
[24] T. Kawahara, K. Araki, and S. Toh, Physica D **59**, 79 (1992).
[25] J. J. Rasmussen, J. P. Lynov, J. S. Hesthaven, and G. G. Sutyrin, Plasma Phys. Controlled Fusion **36**, B193 (1994).
[26] G. G. Sutyrin, J. S. Hesthaven, J. P. Lynov, and J. J. Rasmussen, J. Fluid Mech. **268**, 103 (1994).
[27] V. Naulin, K. H. Spatschek, S. Musher, and L. I. Piterbarg, Phys. Plasmas **2**, 2640 (1995).
[28] D. Fyfe and D. Montgomery, Phys. Fluids **22**, 246 (1979).
[29] H. Okuda, T. Sato, A. Hasegawa, and R. Pellat, Phys. Fluids **23**, 1965 (1980).
[30] M. Makino, T. Kamimura, and T. Sato, J. Phys. Soc. Jpn. **50**, 954 (1981).
[31] J. C. McWilliams, J. Fluid Mech. **146**, 21 (1984).
[32] V. D. Larichev and J. C. McWilliams, Phys. Fluids A **3**, 938 (1991).
[33] N. Kukharkin, S. A. Orszag, and V. Yakhot, Phys. Rev. Lett. **75**, 2486 (1995).
[34] K. H. Spatschek, E. W. Laedke, Chr. Marquardt, S. Musher, and H. Wenk, Phys. Rev. Lett. **64**, 3027 (1990).
[35] A. R. Gourlay and J. Ll. Morris, J. Comput. Phys. **5**, 229 (1970).
[36] A. Arakawa, J. Comput. Phys. **1**, 119 (1966).
[37] M. Prakash, C. K. Chu, and A. Hasegawa, Phys. Fluids **29**, 2426 (1986).
[38] P. S. Marcus, Nature (London) **331**, 693 (1988).
[39] J. Sommeria, S. D. Meyers, and H. L. Swinney, Nature (London) **331**, 689 (1988).
[40] G. P. Williams, J. Atmos. Sci. **35**, 1399 (1978).
[41] R. Peyret and T. D. Taylor, *Computational Methods for Fluid Flow* (Springer, New York, 1985).
[42] D. U. Von Rosenberg, *Methods for the Numerical Solution of Partial Differential Equations* (Elsevier, New York, 1969), Appendix C, p. 116.
[43] S. Benkadda, T. Dudok de Wit, A. Verga, A. Sen, ASDEX Team and X. Garbet, Phys. Rev. Lett. **73**, 3403 (1994).
[44] M. Endler, H. Niedermeyer, L. Giannone, E. Holzhauer, A. Rudyj, G. Theimer, N. Tsois, and ASDEX team, Nucl. Fusion **35**, 1307 (1995).
[45] G. J. J. Botha, Ph.D. thesis, University of London, April 1997.
[46] R. H. Kraichnan and D. Montgomery, Rep. Prog. Phys. **43**, 547 (1980).
[47] M. Wakatani, K. Watanabe, H. Sugama, and A. Hasegawa, Phys. Fluids B **4**, 1754 (1992).
[48] P. W. Terry and D. E. Newman, Phys. Fluids B **5**, 2080 (1993).
[49] V. I. Petviashvili and O. A. Pokhotelov, Sov. J. Plasma Phys. **12**, 651 (1986).